Ion beam assisted deposition of a thin film metallic glass

Vrishank Jambur[a], Zijian Wang[a], John Sunderland[a], Soohyun Im[a], Xuanxin Hu[a], Sakiru Akinyemi[a], John H. Perepezko[a], Paul M. Voyles[a], and Izabela Szlufarska[a]*

[a] *Department of Materials Science and Engineering, University of Wisconsin - Madison, Madison, USA.*

*Corresponding author:

Prof. Izabela Szlufarska

Materials Science and Engineering,

1509 University Avenue,

Madison, WI 53706

Email: szlufarska@wisc.edu

Abstract

We have used ion beam assisted deposition to modify the properties of a thin film $Pd_{77.5}Cu_6Si_{16.5}$ metallic glass without altering the composition. By irradiating the film surface during deposition, the mobility of surface atoms is enhanced, leading to the development of atomically smooth films with increased hardness and kinetic stability. Further, increasing the ion beam energy changes the crystallization pathways in the metallic glass films, pointing to changes in as-deposited structure. This approach to tune the properties of metallic glass films may unlock access to previously unobserved structural states.

Keywords: metallic glass, vapor deposition, mechanical properties, stability, thin films

1. Introduction

Thin film metallic glasses (TFMGs) are excellent candidates to be used as coatings in a variety of applications such as biomedical implants, surgical equipment, semiconductor packaging and flexible electronics due to their good biocompatibility, antimicrobial properties, high strength, and high elastic limit along with resistance to wear, fatigue, and corrosion [1–3]. TFMGs allow exploitation of the unique properties associated with the amorphous structure of metallic glasses (MGs) over a large composition space without having to worry about the glass forming ability, as is the case for metallic glasses in a bulk form.

Although the first TFMGs were synthesized by solid state amorphization of multi-layer films [4], physical vapor deposition (PVD) has emerged as the preferred synthesis route. The interest in PVD synthesized TFMGs increased considerably after Swallen *et al.* [5] demonstrated that PVD could yield organic glasses with enhanced stability. They found higher kinetic and thermodynamic stability in organic glasses deposited at a substrate temperature slightly below the glass transition temperature of an ordinary melt

quenched glass. These glasses were referred to as “ultrastable” because such high stability is practically unattainable in conventional liquid cooled glasses. Following this discovery, there were several reports of the use of PVD to synthesize inorganic glasses such as oxide and metallic glasses with increased stability and hardness[6–18]. Increased stability for TFMGs in the form higher glass transition temperatures and hardness is particularly useful in applications such as coatings since it would allow higher operating temperatures as well as improve wear resistance[19].

The PVD process has many tunable parameters that can affect the properties of the deposited film. However, the only process parameters that have been shown to influence stability are the substrate temperature and the deposition rate. In general, higher substrate temperatures (around $0.8T_g$, where T_g is the glass transition temperature of the ordinary glass) or lower deposition rates have been found to result in MGs with higher stability. Swallen *et al.* [5] explained that all the atoms or molecules in the film would have been in a mobile surface layer [20–25] at some point during the deposition process, where they would have had the ability to move around and find more stable configurations before being buried under the surface. Elevated deposition temperatures enhance surface mobility whereas lower deposition rates increase the surface residence time, allowing surface atoms or molecules to find more stable configurations. Either way, the key to increasing the stability of glasses is believed to be the higher mobility of the atoms or molecules at the surface. This reasoning was backed by Berthier *et al.* [26] who used molecular dynamics (MD) simulations to separate the surface dynamics from bulk dynamics in a Lennard-Jones glass and directly demonstrated how enhanced surface mobility is responsible for the higher stability of vapor deposited glasses.

Considering the importance of surface mobility in controlling stability, we have identified an alternate route to synthesize TFMGs using ion beam assisted deposition

(IBAD). This process involves the bombardment of the growing film with ions to modify its structure and properties. IBAD is commonly used to tune residual stresses, substrate adhesion, surface roughness, hardness, refractive index, magnetic anisotropy, etc. [27] in crystalline films. This process is different from what Luo *et al.* [11] refer to as IBAD. In their method, the ion beam is directed at a target from which atoms are sputtered towards the substrate at very low deposition rates. We have used ion beams directed at the surface of a growing film according to the conventional definition of IBAD and obtained TFMGs with increased kinetic stability and hardness. Our approach is also different from that of Kobata and Miura [28] who used a technique called unbalanced magnetron sputtering to irradiate the surface of a growing metallic glass film. While they implant Ar^+ ions into the TFMG to change its composition and properties, we irradiate the growing film with relatively low energy Ar^+ ions to transfer kinetic energy to the surface atoms and increase their mobility, while avoiding implantation of the incident ions. In comparison to other approaches to enhance the stability of TFMGs, IBAD offers some key advantages including not needing to heat the substrate, and not needing to use extremely low deposition rates and therefore substantially reducing the time needed to grow films.

2. Methods

MG films were prepared using a DC magnetron sputtering system retrofitted with a single beam ion source acquired from Scion Plasma. Fig.1 shows a schematic of this setup. The sputter target was 2 inches in diameter with a separation of 15 cm from the substrate which was on a rotating stage (~30 rpm). The films were grown under three distinct conditions: (1) without ion beam irradiation (*No IB*), (2) ion source activated at an ion energy of 90 eV with ion gun current of 0.19 A (*90eV IB*), and (3) ion energy of 180 eV with ion gun current of 0.32 A (*180eV IB*). The ion beam was 1 inch in diameter with an angle of ion incidence was maintained constant at 70° with respect to the substrate normal

(Fig.1). The sputtering process employed a single alloy target of composition $Pd_{77.5}Cu_6Si_{16.5}$, obtained from ACI Alloys Inc. This composition was chosen due to the inert nature of its major component Pd that makes is more resistant to oxidation compared to other glass forming alloys such as those containing Zr. The sputtering power remained fixed at 50 W, and the deposition was conducted at room temperature for a duration of 100 minutes to achieve film thickness in the range of 1.2-1.5 μm with deposition rate in the range 0.2-0.25 nm/s. The base pressure in the deposition chamber was below 2.7×10^{-5} Pa and the operating pressure of the Ar process gas was maintained at 0.4 Pa. Si wafers were cleaved into pieces with dimensions 2 cm x 2 cm and used as substrates to grow samples for nanoindentation and other characterization while NaCl discs (1 inch diameter) served as the substrates for films employed in differential scanning calorimetry (DSC) experiments. Before deposition, the cleaved Si substrates were cleaned by 5 minutes of ultrasonication in ethanol followed by another five minutes of ultrasonication in DI water. The quenched *Ribbon* sample was made by melt-spinning on a Cu wheel with a speed of 40 m/s and in an Ar atmosphere.

The composition of the films was measured using X-ray photoelectron spectroscopy (XPS) performed on a Thermo Scientific K alpha system using an Al K-α source. To remove the oxidized surface layer, the sample was ion-milled for 60s to a depth of 10 nm using a 2000eV Ar^+ ion beam. The ion milling was repeated to measure the composition of the film up to a depth of 40 nm in 10 nm steps. X-ray diffraction (XRD) was performed on a Bruker D8 Discover instrument with a Cu K-α source with a grazing incidence geometry. Scanning electron microscopy (SEM) elemental distribution maps were obtained by energy dispersive spectroscopy (EDS) on a Zeiss Gemini 300 FESEM using a 20kV accelerating voltage.

The transmission electron microscopy (TEM) specimens were cleaned using a plasma cleaner (ibss GV10x DS Asher plasma cleaner) for 3 min under 20W to remove hydrocarbon contamination before inserting into the TEM column. TEM EDS was performed using a scanning transmission electron microscope (STEM, FEI Titan G2 80-200). The microscope was operated at an acceleration voltage of 200kV with a 70μm C2 aperture and the EDS acquisition was performed with dwell time of 1000ms.

The surface morphology of the films was characterized by atomic force microscopy (AFM) on a Bruker Icon instrument. Nanoindentation was performed on a Hysitron TI 950 Triboindenter in the load-controlled mode, with a Berkovich tip. The maximum load was selected such that the indent depth didn't exceed 10% of the film thickness to avoid substrate effects on the measured nanomechanical properties. The glass transition and crystallization of the samples was examined using a Perkin Elmer Diamond Differential Scanning Calorimeter (DSC). The NaCl substrates were dissolved in water to obtain free standing films for DSC. Measurements were done in an Ar atmosphere at a heating rate of 20 K/min. Residual stress in the films was determined by measuring wafer curvature on a Tencor FLX-2320 instrument.

Threshold displacement energies (E_{TD}) for Pd and Si surface atoms were calculated by classical MD simulations using the LAMMPS software package [29] and a binary EAM potential [30]. A melt-quenched glass with composition $Pd_{82}Si_{18}$ was obtained using the procedure described in [31]. The quenched glass was used to calculate the E_{TD} with the following steps. First, the system was equilibrated to a temperature of 300 K in the NVE ensemble with periodic boundary conditions in two directions and a free surface along one direction. Next, atoms on the free surface were selected at random and assigned kinetic energies. The system was then allowed to equilibrate again in the

NVE ensemble for 1ps and the displacement of the selected atoms was determined. A displacement cutoff equal to the nearest neighbor distance from the pair distribution function was used to determine whether an atom was permanently displaced. The reported E_{TD} is an average of 20-30 atoms of each type. Recoil energies for varying incident ion energies were determined using the SRIM (Stopping and Range of Ions in Matter) package [32].

3. Results and discussion

The compositions of the films and the quenched *Ribbon* sample were measured using XPS (Fig.2) and were confirmed to be close to the nominal composition of $Pd_{77.5}Cu_6Si_{16.5}$ (within XPS accuracy of 5% [33]) for all the samples. The surfaces of the films seem to be oxidized while the bulk is free of oxidation. Absence of Ar in the *90eV IB* and *180eV IB* films indicates that the ion energies chosen for IBAD were low enough to avoid implantation of Ar^+ ions in the films. Diffraction patterns obtained from a laboratory XRD system are shown in Fig.3. All the samples show a single broad diffraction peak that indicates a fully amorphous structure. Differences in the position of the peak indicate slight variations in the atomic level topological and chemical ordering in the samples. TEM-SAED patterns with amorphous halos (Fig. A1) rule out the presence of nanocrystals, confirming that all the samples are completely amorphous.

Figs. 4a-c show the surface morphology of the films obtained from AFM. The *No IB* film has an RMS roughness of 1.7 nm and has a nanostructure consisting of clusters with diameters in the range of 20-40 nm. The *90eV IB* and *180eV IB* films have atomically smooth surfaces with roughness of 0.18 nm and 0.23 nm, respectively, and appear to have a homogenous surface with no distinct features. Such a transition from a nanostructured to a homogenous surface morphology in vapor deposited films is generally attributed to an increased mobility of surface atoms [34–36]. The nanostructured surface morphology

in the *No IB* film is a consequence of columnar growth also known as the Volmer-Weber or island growth mode [37]. This film growth mode occurs when the deposited atoms prefer to bind with each other rather than the substrate atoms, due to high interfacial energies between the film and substrate. Consequently, the adatoms arriving at the substrate form islands to minimize the interfacial area. As the islands grow, the subsequently arriving adatoms will have a higher probability of being deposited on top of the relatively tall islands which will continue to grow at the expense of the shorter islands in their shadow. This shadowing effect results in the growth of columnar regions with relatively high atomic densities separated by boundaries with low atomic density. However, if the atoms arriving at the surface on top of the taller columns have sufficient mobility, they will diffuse to the surrounding areas with low atomic densities resulting in a smooth surface [36]. Based on this reasoning, the presence of smooth surfaces seen in the *90eV IB* and the *180eV IB* films is consistent with increased surface mobility during deposition.

Elastic modulus measured by nanoindentation (Fig. 5a) shows a 33% increase from the quenched *Ribbon* sample to the *No IB* film. The ion beam energy does not seem to have any obvious effect on the elastic modulus of the films with the *90eV IB* film showing a 4.4% decrease with respect to the *No IB* film while the *180eV IB* film shows no change outside of experimental uncertainty. A higher elastic modulus is generally a consequence of a shorter average interatomic distances and a denser glass structure [13]. This suggests that the films have a higher density than the *Ribbon* sample and that the density does not change much with the use of IBAD. Comparing nanoindentation hardness (Fig. 5b), we see a gradual increase going from the *Ribbon* sample to the *No IB* film followed by the *90eV IB* film and then the *180eV IB* film. Overall, there is an 11% increase in hardness from the *Ribbon* to the *180eV IB* film. Among the films, there is a

187 5.3% increase in hardness from the *No IB* to the *180eV IB* film. Unlike the elastic
188 modulus, the hardness, which is a measure of a material's resistance to deformation, is
189 influenced not only by the interatomic distances but also other factors like the surface
190 roughness, morphology, and microstructure. The morphology of the *No IB* film consists
191 of clusters separated by boundaries containing loosely packed atoms with excess free
192 volume. These boundary regions allow the easy activation of shear bands and offer lower
193 resistance to plastic deformation, resulting in lower hardness in the *No IB* film compared
194 to the films grown using IBAD where the nanograined structure is eliminated due to
195 enhanced surface mobility during film growth. Higher hardness has also been connected
196 to increased stability in TFMGs [11].

197 Heat flow traces from the DSC heating scan of all the samples are shown in Fig.
198 6a. All the traces exhibit an endothermic step corresponding to the glass transition around
199 360 ^{o}C and an exothermic peak corresponding to crystallization at around 400 ^{o}C,
200 agreeing with values reported in literature [38]. However, there is a striking difference
201 between the DSC traces of the *Ribbon* sample and the films prior to the glass transition.
202 The *Ribbon* has a relatively flat heat flow curve prior to the onset of glass transition
203 whereas the films appear to be undergoing an exothermic change as seen by the
204 downward sloping heat flow curve. Such an exothermic change usually corresponds to
205 relaxation of the glass towards a more stable thermodynamic state [39]. This trend would
206 suggest that the as-deposited state of the films is thermodynamically less stable compared
207 to the *Ribbon* sample, which does not exhibit an exothermic slope prior to the glass
208 transition. Lower thermodynamic stability in MGs is sometimes associated with less
209 dense structures and lower elastic moduli [13]. This explanation would be in contradiction
210 to the significantly higher nanoindentation elastic modulus seen in the films compared to
211 the *Ribbon* sample. However, Yu *et al*. [9], who were among the first to report

ultrastability in MGs, also observed that the ultrastable MG with the higher elastic modulus had a higher enthalpy and was less thermodynamically stable than the quenched MG. In their study, they referred to the ultrastable MG as the one that had the higher kinetic stability (higher glass transition temperature), rather than thermodynamic stability and concluded that the kinetic stability of metallic glasses is not always coupled with their thermodynamic stability. While our results seem be similar to that of Yu *et al*. [9], we should note that the inference about the thermodynamic stability of our samples is somewhat speculative, since it is not possible to draw reliable conclusions about the relative thermodynamic stabilities from just comparing the heat flow curves without establishing a baseline and calculating the difference in enthalpies with respect to a common reference state. Another plausible explanation could be that the observed exothermic behavior in the DSC traces of the films is from residual stresses developed in the films during the deposition process. It is not surprising that the films will develop significant residual stresses given their sizeable thickness [2]. The idea that the films possess residual stresses is supported by the observed curling up of the films upon separation from the substrate (Fig. 7). Wafer curvature measurements confirm the presence of compressive stresses in the films but do not indicate significant differences between the *No IB* (101.9MPa), *90eV IB* (124.1MPa), and the *180eV IB* (114.9MPa) films. However, it must be noted that the wafer curvature measurements were conducted with films grown on 3 inch diameter Si substrates while the ion beam used during the deposition of the films was only 1 inch in diameter. This means that large parts of the wafer would not have interacted with Ar^+ ions. An alternate FIB based method (described in Appendix) was also used to measure the residual stresses in films grown on the smaller 2 cm x 2 cm Si substrates. These measurements (Fig. A2) also indicate compressive residual stresses in all the films with similar magnitude as the stresses measured using the

wafer curvature method. While these compressive residual stresses may be one of the reasons for the exothermic slopes seen in the DSC traces, they are less likely to have any influence on the elastic modulus and hardness of the films, which are an order of magnitude higher than the measured residual stress.

The glass transition temperature reported for MGs in literature usually corresponds to the onset of the glass transition on heating. However, the steep curvature in the DSC traces of our films makes it challenging to measure the onset T_g. Instead, we report the midpoint glass transition temperature, which corresponds to the midpoint in the endothermic step in the glass transition and can be determined without ambiguity from the peak in the derivative of the heat flow curve (Figs. 6b-e). We find that the T_g of the *Ribbon* sample (T_g = 367 ºC) as well as of the *No IB* (T_g = 366 ºC) and *90eV IB* (T_g = 368 ºC) films all lie within a range of 2 ºC and can be considered to have almost identical kinetic stability. Only the *180eV IB* (T_g = 372 ºC) film appears to show a slightly higher T_g indicating a modest increase in kinetic stability with respect to the other samples. The endothermic step that corresponds to the transition from the glassy state to the supercooled liquid state appears to be the most pronounced for the *180eV IB* film, another indication of increased kinetic stability.

The crystallization peaks of all the samples have onset temperatures (T_x) very close to each other. Specifically, the *Ribbon* sample (T_x = 398 ºC), *No IB* film (T_x = 400 ºC), and the *90 eV IB* (T_x = 399 ºC) film are again within a range of 2 ºC, and the 180 eV *IB* (T_x = 402 ºC) is only marginally higher. However, the peak crystallization temperatures show a larger variation between the samples. The *Ribbon* sample (T_{xp} = 419 ºC) has the highest T_{xp} followed by the *180eV IB* sample (T_{xp} = 414 ºC). The *No IB* film (T_{xp} = 403 ºC) and the *90eV IB* film (T_{xp} = 404 ºC) have the lowest T_{xp} and the narrowest

crystallization peaks. The differences in the T_{xp} of the samples indicate differences in crystallization pathways, which is confirmed by the diffraction patterns obtained after crystallization (Fig. 3b). The *Ribbon* sample with the highest T_{xp} has the most distinct diffraction peaks among the samples. However, this is not unexpected since melt-quenched MGs with the same composition as vapor deposited MGs have been shown to select different crystallization pathways due differences in their topological and chemical medium range orders (MRO) [40]. What is more surprising is the difference in the diffraction patterns of the films, with the *180eV IB* film having clearly different peaks compared to the *No IB* and *90eV IB* films, where the latter two films have almost identical diffraction patterns (Fig. 3b). This means that the use of higher energy ions during IBAD alters the structure or the composition of the glass in a way that results in a different crystallization pathway. While ion irradiation has been shown to result in segregation and crystallization in MGs [41,42], such processes usually require the use of heavy ions with high energies. Furthermore, we have already confirmed that our samples are fully amorphous using XRD to rule out the possibility of crystallization induced by the ion beam. In addition, we have also checked for elemental segregation at different length scales using SEM as well as TEM EDS mapping (Fig. 8 and Fig. 9, respectively). The EDS maps at the micrometer and nanometer length scales show no evidence of segregation in any of the films. All these results suggest that the reason for the different crystallization pathway in the *180eV IB* film could be changes in the topological and chemical medium- or short-range orders at length scales that cannot be observed in the XRD or EDS experiments.

During the IBAD process, the Ar^+ ions incident on the surface of the growing film will undergo collisions with the atoms on the surface and transfer kinetic energy. Fig.10a and Fig. 10b show the energy absorbed by the atoms in the film (E_{recoil}) as a function of

their depth from the surface for incident ion energies of 90eV and 180eV, respectively. In both cases the energy of the incident ions is almost entirely transferred to atoms at the surface layer. The minimum kinetic energy needed to permanently displace atoms from their initial position is called the threshold displacement energy (E_{TD}). If E_{recoil} is less than the E_{TD}, the atom will not be displaced, but instead will undergo oscillations around its equilibrium position, which may result in local heating. On the other hand, if E_{recoil} is higher than its E_{TD}, the atom will be displaced, resulting in a collision cascade. We find that E_{recoil} barely exceeds E_{TD} for the surface Pd and Si atoms for the 90eV ion beam (Fig. 10a) whereas E_{recoil} is well over E_{TD} for the 180eV ion beam (Fig. 10b). This means that the mode of interaction between the ion beam and the film changes with increasing ion beam energy. At low ion energies, the incident ions displace very few surface atoms and most of the energy from the ions is dissipated through local heating. At higher ion energies, the incident ions can displace several surface atoms and cause collision cascades, leading to significant alterations in the topological and chemical MRO. This could be the reason for the different crystallization pathway in the *180eV IB* film. It is interesting to note that Giordano and Ruta [43] have reported the presence of an additional secondary relaxation process in a glass of the same composition as in the current study. This additional secondary relaxation was said to be related to the onset of nucleation or phase separation prior to crystallization and it was found to take place upon annealing at high temperatures. It is possible that the higher energy ions used in IBAD also activate the same or a similar relaxation process leading to the structural or chemical ordering as a precursor to crystallization.

4. Conclusion

We have discovered that IBAD is a promising technique for synthesizing TFMGs and controlling their properties. We have obtained atomically smooth surfaces along with

modest enhancements in the kinetic stability and hardness of TFMGs grown using IBAD. At relatively higher ion energies, IBAD has also significantly altered the crystallization pathway of the films, pointing to difference in the as-deposited structure, probably in the form of chemical or topological MRO. This finding suggests that IBAD may enable access to structural states that cannot be achieved through varying conventional deposition parameters, such as substrate temperature and deposition rates. With further exploration and tuning of the ion beam parameters, this process holds significant potential for the synthesis of TFMGs with even higher kinetic stability and hardness, for use as coatings in several engineering applications. From a scientific standpoint, we have decoupled the influence of surface mobility from that of bulk mobility, and provided further evidence to support the hypothesis that increased surface mobility plays a crucial role in the heightened stability of vapor-deposited glasses.

Acknowledgements

This research was primarily supported by NSF through the University of Wisconsin Materials Research Science and Engineering Center (DMR-1720415). Partial support for final analysis and manuscript preparation was provided by DMR-2309000.

Disclosure statement

The authors declare no potential conflict of interest.

References

[1] J.P. Chu, J.C. Huang, J.S.C. Jang, Y.C. Wang, P.K. Liaw, Thin film metallic glasses: Preparations, properties, and applications, Jom 62 (2010) 19–24. https://doi.org/10.1007/s11837-010-0053-3.

[2] J.P. Chu, J.S.C. Jang, J.C. Huang, H.S. Chou, Y. Yang, J.C. Ye, Y.C. Wang, J.W. Lee, F.X. Liu, P.K. Liaw, Y.C. Chen, C.M. Lee, C.L. Li, C. Rullyani, Thin film

metallic glasses: Unique properties and potential applications, Thin Solid Films 520 (2012) 5097–5122. https://doi.org/10.1016/j.tsf.2012.03.092.

[3] P. Yiu, W. Diyatmika, N. Bönninghoff, Y.C. Lu, B.Z. Lai, J.P. Chu, Thin film metallic glasses: Properties, applications and future, J Appl Phys 127 (2020). https://doi.org/10.1063/1.5122884.

[4] R.B. Schwarz, W.L. Johnson, Formation of an amorphous alloy by solid-state reaction of the pure polycrystalline metals, Phys Rev Lett 51 (1983) 415–418. https://doi.org/10.1103/PhysRevLett.51.415.

[5] S.F. Swallen, K.L. Kearns, M.K. Mapes, Y.S. Kim, R.J. McMahon, M.D. Ediger, T. Wu, L. Yu, S. Satija, Organic glasses with exceptional thermodynamic and kinetic stability, Science (1979) 315 (2007) 353–356. https://doi.org/10.1126/SCIENCE.1135795/SUPPL_FILE/SWALLEN_SOM.PDF.

[6] C. Tangpatjaroen, K. Bagchi, R.A. Martínez, D. Grierson, I. Szlufarska, Mechanical Properties of Structure-Tunable, Vapor-Deposited TPD Glass, J. Phys. Chem. C 122 (2018). https://doi.org/10.1021/acs.jpcc.8b09718.

[7] V. Jambur, M. Molina-Ruiz, T. Dauer, D. Horton-Bailey, R. Vallery, D. Gidley, T.H. Metcalf, X. Liu, F. Hellman, I. Szlufarska, Temperature effects on the structure and mechanical properties of vapor deposited a-SiO2, J Non Cryst Solids 587 (2022) 121588. https://doi.org/10.1016/J.JNONCRYSOL.2022.121588.

[8] L. Yang, G. Vajente, M. Fazio, A. Ananyeva, G.L. Billingsley, A. Markosyan, R. Bassiri, K. Prasai, M.M. Fejer, M. Chicoine, F. Schiettekatte, C.S. Menoni, Enhanced medium-range order in vapor-deposited germania glasses at elevated temperatures, Sci Adv 7 (2021). https://doi.org/10.1126/sciadv.abh1117.

[9] H. Bin Yu, Y. Luo, K. Samwer, Ultrastable metallic glass, Advanced Materials 25 (2013) 5904–5908. https://doi.org/10.1002/ADMA.201302700.

[10] D.J. Magagnosc, G. Feng, L. Yu, X. Cheng, D.S. Gianola, Isochemical control over structural state and mechanical properties in Pd-based metallic glass by sputter deposition at elevated temperatures, APL Mater 4 (2016) 086104. https://doi.org/10.1063/1.4960388.

[11] P. Luo, C.R. Cao, F. Zhu, Y.M. Lv, Y.H. Liu, P. Wen, H.Y. Bai, G. Vaughan, M. Di Michiel, B. Ruta, W.H. Wang, Ultrastable metallic glasses formed on cold substrates, Nat Commun 9 (2018) 1–7. https://doi.org/10.1038/s41467-018-03656-4.

[12] Q. Sun, D.M. Miskovic, K. Laws, H. Kong, X. Geng, M. Ferry, Transition towards ultrastable metallic glasses in Zr-based thin films, Appl Surf Sci 533 (2020) 147453. https://doi.org/10.1016/J.APSUSC.2020.147453.

[13] S. V Muley, C. Cao, D. Chatterjee, C. Francis, F.P. Lu, M.D. Ediger, J.H. Perepezko, P.M. Voyles, Varying kinetic stability, icosahedral ordering, and mechanical properties of a model Zr-Cu-Al metallic glass by sputtering, Phys Rev Mater 5 (2021) 33602. https://doi.org/10.1103/PhysRevMaterials.5.033602.

[14] G.B. Bokas, L. Zhao, D. Morgan, I. Szlufarska, Increased stability of CuZrAl metallic glasses prepared by physical vapor deposition, J Alloys Compd 728 (2017) 1110–1115. https://doi.org/10.1016/j.jallcom.2017.09.068.

[15] M.X. Li, Y.T. Sun, C. Wang, L.W. Hu, S. Sohn, J. Schroers, W.H. Wang, Y.H. Liu, Data-driven discovery of a universal indicator for metallic glass forming ability, Nat Mater 21 (2022) 165–172. https://doi.org/10.1038/s41563-021-01129-6.

[16] P. Luo, F. Zhu, Y.M. Lv, Z. Lu, L.Q. Shen, R. Zhao, Y.T. Sun, G.B.M. Vaughan, M. Di Michiel, B. Ruta, H.Y. Bai, W.H. Wang, Microscopic Structural Evolution during Ultrastable Metallic Glass Formation, ACS Appl Mater Interfaces 13 (2021) 40098–40105. https://doi.org/10.1021/acsami.1c10716.

[17] M. Jain, A. Sharma, K. Pajor, K. Wieczerzak, N.M. della Ventura, X. Maeder, J.J. Kruzic, B. Gludovatz, J. Michler, Mechanical properties and thermal stability of thin film metallic glass compared to bulk metallic glass from ambient to elevated temperatures, J Alloys Compd 960 (2023). https://doi.org/10.1016/j.jallcom.2023.170728.

[18] J. Antonowicz, P. Zalden, K. Sokolowski-Tinten, K. Georgarakis, R. Minikayev, A. Pietnoczka, F. Bertram, M. Chaika, M. Chojnacki, P. Dłużewski, K. Fronc, A.L. Greer, C. Jastrzębski, D. Klinger, C. Lemke, O.M. Magnussen, B. Murphy, K. Perumal, U. Ruett, K.J. Warias, R. Sobierajski, Devitrification of thin film Cu–Zr metallic glass via ultrashort pulsed laser annealing, J Alloys Compd 887 (2021). https://doi.org/10.1016/j.jallcom.2021.161437.

[19] Z. Liao, N. Hua, W. Chen, Y. Huang, T. Zhang, Correlations between the wear resistance and properties of bulk metallic glasses, Intermetallics (Barking) 93 (2018) 290–298. https://doi.org/10.1016/j.intermet.2017.10.008.

[20] L. Zhu, C.W. Brian, S.F. Swallen, P.T. Straus, M.D. Ediger, L. Yu, Surface Self-Diffusion of an Organic Glass, Phys Rev Lett 106 (2011) 256103–256104. https://doi.org/10.1103/PhysRevLett.106.256103.

[21] W. Zhang, L. Yu, Surface Diffusion of Polymer Glasses, Macromolecules 49 (2016) 731–735. https://doi.org/10.1021/acs.macromol.5b02294.

[22] Y. Zhang, R. Potter, W. Zhang, Z. Fakhraai, Using tobacco mosaic virus to probe enhanced surface diffusion of molecular glasses, Soft Matter 12 (2016) 9115. https://doi.org/10.1039/c6sm01566b.

[23] C.R. Cao, Y.M. Lu, H.Y. Bai, W.H. Wang, High surface mobility and fast surface enhanced crystallization of metallic glass, Appl Phys Lett 107 (2015) 141606. https://doi.org/10.1063/1.4933036.

[24] K.L. Ngai, S. Capaccioli, C.R. Cao, H.Y. Bai, W.H. Wang, Quantitative explanation of the enhancement of surface mobility of the metallic glass Pd40Cu30Ni10P20 by the Coupling Model, J Non Cryst Solids 463 (2017) 85–89. https://doi.org/10.1016/J.JNONCRYSOL.2017.03.002.

[25] C.R. Cao, L. Yu, J.H. Perepezko, Surface dynamics measurement on a gold based metallic glass, Appl Phys Lett 116 (2020) 231601. https://doi.org/10.1063/5.0007838.

[26] L. Berthier, P. Charbonneau, E. Flenner, F. Zamponi, Origin of Ultrastability in Vapor-Deposited Glasses, (2017). https://doi.org/10.1103/PhysRevLett.119.188002.

[27] J.M.E. Harper, J.J. Cuomo, R.J. Gambino, H.R. Kaufman, Modification of thin film properties by ion bombardment during deposition, Nucl Instrum Methods Phys Res B 7–8 (1985) 886–892. https://doi.org/10.1016/0168-583X(85)90489-6.

[28] J. Kobata, K. ichi Miura, Effects of Ar ion bombardment by unbalanced magnetron sputtering on mechanical and thermal properties of Ti-Cu-Zr-Ni-Hf-Si thin film metallic glass, Mater Des 111 (2016) 271–278. https://doi.org/10.1016/J.MATDES.2016.09.005.

[29] S. Plimpton, Fast Parallel Algorithms for Short-Range Molecular Dynamics, J Comput Phys 117 (1997) 1–42. https://doi.org/10.1006/jcph.1995.1039.

[30] J. Ding, Y.-Q. Cheng, H. Sheng, E. Ma, Short-range structural signature of excess specific heat and fragility of metallic-glass-forming supercooled liquids, Phys Rev B 85 (2012) 060201. https://doi.org/10.1103/PhysRevB.85.060201.

[31] V. Jambur, C. Tangpatjaroen, J. Xi, J. Tarnsangpradit, M. Gao, H. Sheng, J.H. Perepezko, I. Szlufarska, Effects of minor alloying on the mechanical properties of Al based metallic glasses, J Alloys Compd 854 (2021) 157266. https://doi.org/10.1016/j.jallcom.2020.157266.

[32] J.F. Ziegler, M.D. Ziegler, J.P. Biersack, SRIM - The stopping and range of ions in matter (2010), Nucl Instrum Methods Phys Res B 268 (2010) 1818–1823. https://doi.org/10.1016/j.nimb.2010.02.091.

[33] A.G. Shard, Practical guides for x-ray photoelectron spectroscopy: Quantitative XPS, Journal of Vacuum Science & Technology A 38 (2020) 041201. https://doi.org/10.1116/1.5141395.

[34] A.G. Dirks, H.J. Leamy, Columnar microstructure in vapor-deposited thin films, Thin Solid Films 47 (1977) 219–233. https://doi.org/10.1016/0040-6090(77)90037-2.

[35] S.G. Mayr, K. Samwer, Tailoring the surface morphology of amorphous thin films by appropriately chosen deposition conditions, J Appl Phys 91 (2002) 2779–2784. https://doi.org/10.1063/1.1446235.

[36] P. Denis, S.Y. Liu, H.J. Fecht, Growth mode transition in Au-based thin film metallic glasses, Thin Solid Films 665 (2018) 29–35. https://doi.org/10.1016/j.tsf.2018.08.006.

[37] J.E. Greene, Thin Film Nucleation, Growth, and Microstructural Evolution: An Atomic Scale View, in: Handbook of Deposition Technologies for Films and Coatings: Science, Applications and Technology, Elsevier, 2009: pp. 554–620. https://doi.org/10.1016/B978-0-8155-2031-3.00012-0.

[38] Z.P. Lu, H. Tan, Y. Li, S.C. Ng, Correlation between reduced glass transition temperature and glass forming ability of bulk metallic glasses, Scr Mater 42 (2000) 667–673. https://doi.org/10.1016/S1359-6462(99)00417-0.

[39] D. Janovszky, M. Sveda, A. Sycheva, F. Kristaly, F. Zámborszky, T. Koziel, P. Bala, G. Czel, G. Kaptay, Amorphous alloys and differential scanning calorimetry (DSC), Journal of Thermal Analysis and Calorimetry 2021 147:13 147 (2021) 7141–7157. https://doi.org/10.1007/S10973-021-11054-0.

[40] C. Yildirim, M. Kutsal, R.T. Ott, M.F. Besser, M.J. Kramer, Y.E. Kalay, The role of amorphous precursor in phase selection hierarchy in marginal metallic glasses, Mater Des 112 (2016) 479–484. https://doi.org/10.1016/j.matdes.2016.09.060.

[41] M.T. Myers, S. Charnvanichborikarn, C.C. Wei, Z.P. Luo, G.Q. Xie, S.O. Kucheyev, D.A. Lucca, L. Shao, Phase transition, segregation and nanopore formation in high-energy heavy-ion-irradiated metallic glass, Scr Mater 67 (2012) 887–890. https://doi.org/10.1016/j.scriptamat.2012.08.015.

[42] J. Carter, E.G. Fu, M. Martin, G. Xie, X. Zhang, Y.Q. Wang, D. Wijesundera, X.M. Wang, W.K. Chu, S.M. McDeavitt, L. Shao, Ion irradiation induced nanocrystal formation in amorphous Zr55Cu30Al10Ni5 alloy, Nucl Instrum Methods Phys Res B 267 (2009) 2827–2831. https://doi.org/10.1016/j.nimb.2009.05.068.

[43] V.M. Giordano, B. Ruta, Unveiling the structural arrangements responsible for the atomic dynamics in metallic glasses during physical aging, Nat Commun 7 (2016). https://doi.org/10.1038/ncomms10344.

[44] A.M. Korsunsky, M. Sebastiani, E. Bemporad, Residual stress evaluation at the micrometer scale: Analysis of thin coatings by FIB milling and digital image correlation, Surf Coat Technol 205 (2010) 2393–2403. https://doi.org/10.1016/J.SURFCOAT.2010.09.033.

Appendix

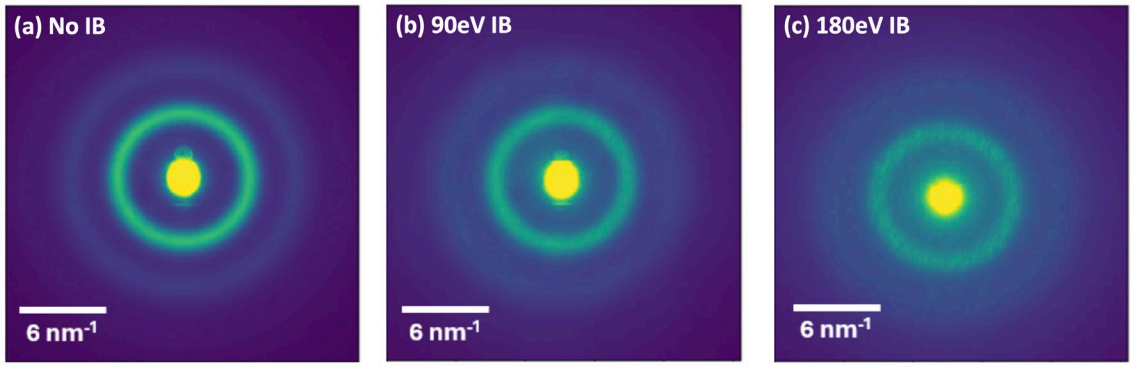

Figure A1. TEM-SAED patterns for (a) *No IB*, (b) *90eV IB*, and (c) *180eV IB* films showing an amorphous halo, confirming the absence of local crystallization.

The averaged nanodiffraction patterns were collected using Direct Electron Celeritas camera with microprobe-mode scanning transmission electron microscopy (STEM; Thermo Fisher Scientific Titan) with 200 keV accelerating voltage. The probe size of the incident beam is about 1 nm, which was formed by a 10 μm C2 aperture and 1.50 mrad convergence half-angle.

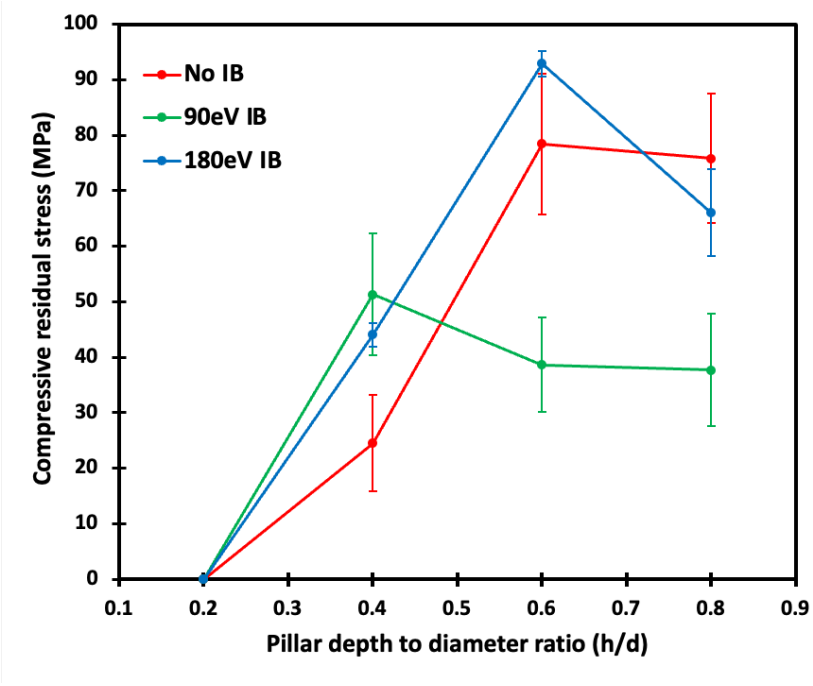

Figure A2. Compressive residual stresses in films measured using FIB based method. Error bars indicate standard deviations.

The residual stresses in the films were measured using a FIB based method. First, a thin Pt layer with the thickness of around 100 nm was deposited on the *No IB*, *90eV IB*, and the *180eV IB* films using an ion beam voltage of 30 kV and current of 20 pA on a Ziess Auriga FIB. The purpose of the Pt layer was to protect the metallic glass films from ion-beam damage during the subsequent steps. Then, a grid of small dots with a diameter of 100 nm, depth of 100 nm, and spacing of 400 nm was milled on the Pt layer using an ion beam voltage of 30 kV and current of 5 pA. The grid was used as a landmarking feature on the surface of the samples. The samples were then moved to a FEI Helios Plasma FIB for the remaining steps. Next, ring-core milling was performed with an inner diameter of 1 μm and an outer diameter of 5 μm using an ion beam voltage of 30 kV and current of 15 pA. An outer-to-inner path was followed during milling to avoid material redeposition over the central pillar. The milling was done in depth increments of 250 nm. Between the milling steps, SEM images of the central pillar were recorded for subsequent digital image correlation (DIC) analysis. DIC

514 analysis of the SEM images was carried out using a Matlab implementation of the DIC
515 procedure described in [44], making use of the library function cpcorr.
516
517 **Figures:**
518

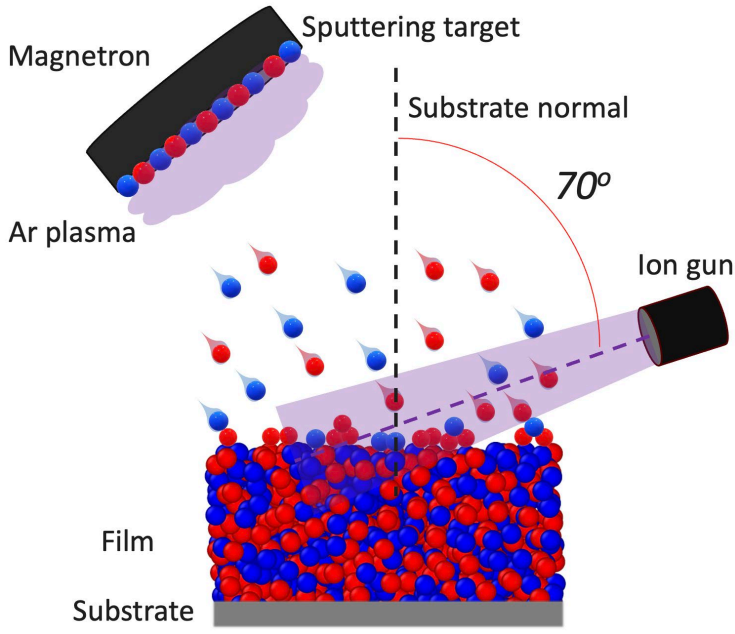

519
520 Figure 1. Schematic of the IBAD setup.
521
522

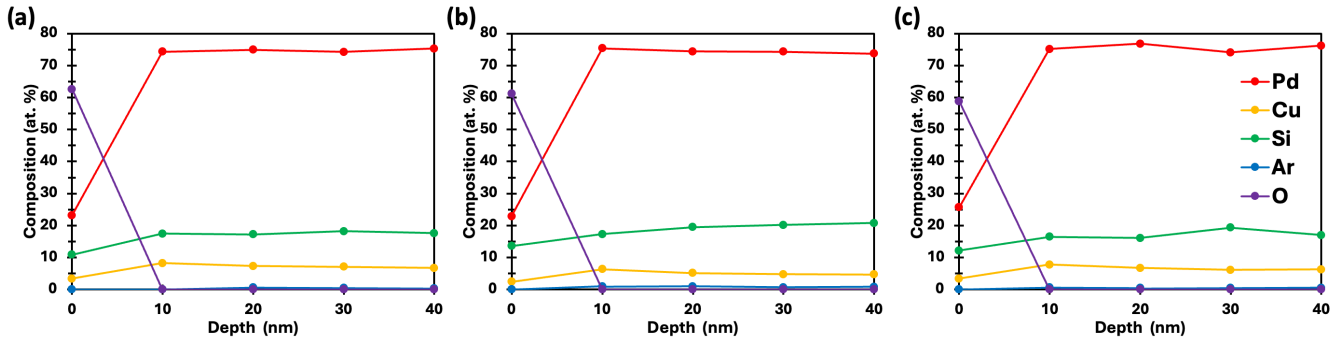

523
524 Figure 2. Compositions of (a) *No IB*, (b) *90eV IB*, and (c) *180eV IB* films at increasing
525 depths from surface measured using XPS.
526

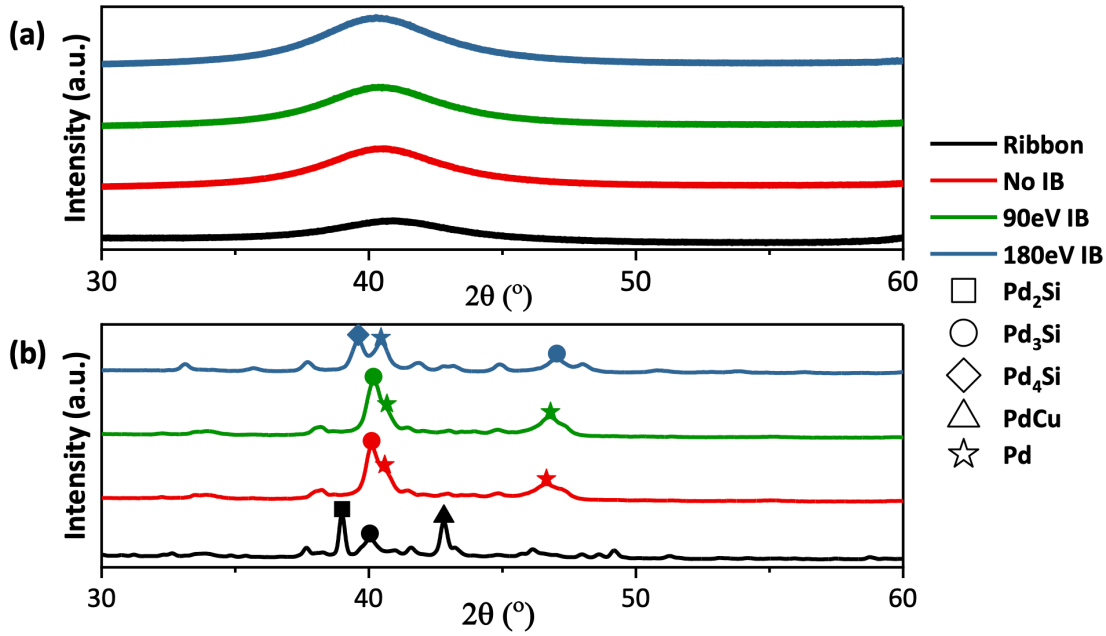

Figure 3. XRD patterns of (a) *as deposited* and (b) *crystallized* films and ribbon.

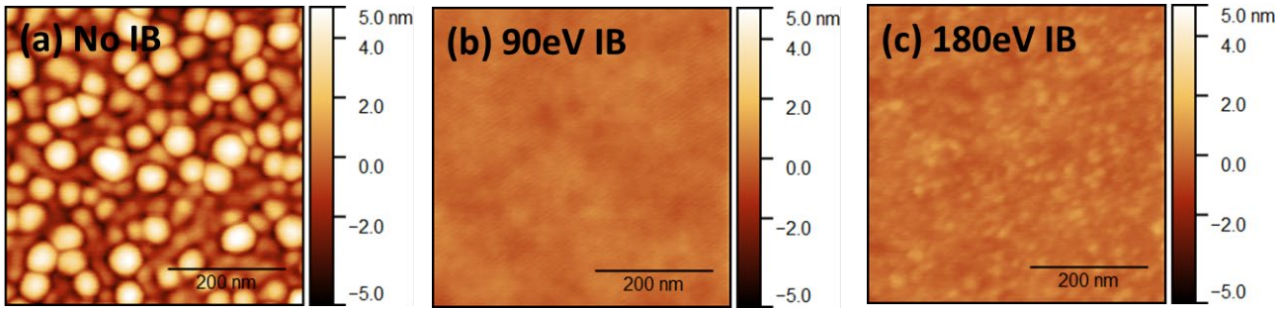

Figure 4. Surface morphologies of (a) *No IB*, (b) *90eV IB*, and (c) *180eV IB* films from AFM.

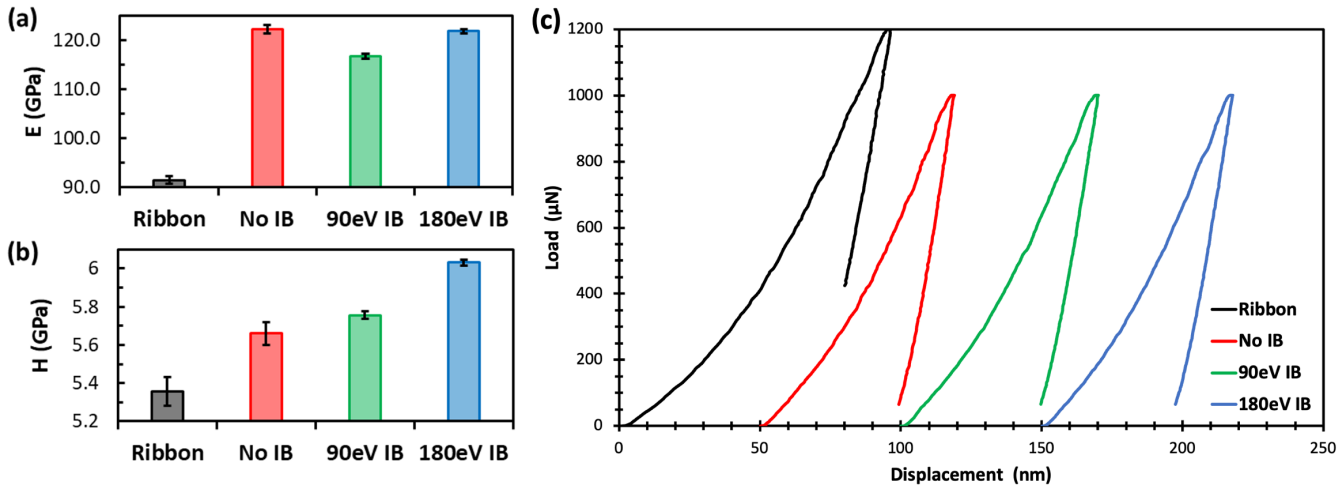

538

539 Figure 5. (a) Elastic modulus and (b) Hardness measured by nanoindentation. Error bars

540 represent standard error in mean from 30 measurements. (c) Representative

541 nanoindentation load-displacement curves showing serrations indicative of shear band

542 activity during deformation.

543

544

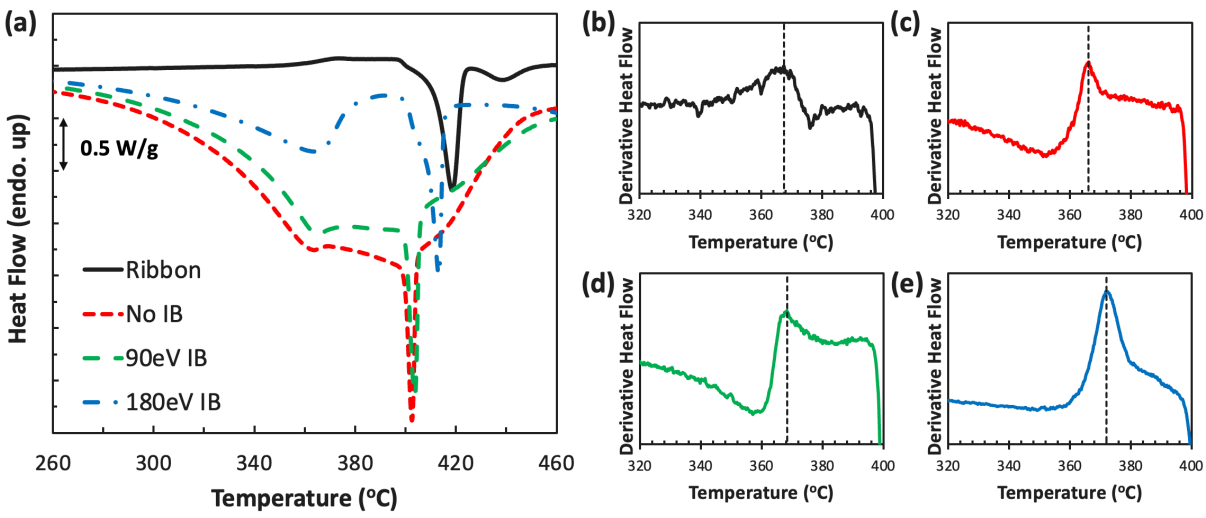

545

546 Figure 6. (a) DSC heat flow traces from heating scans; Derivative of heat flow traces for

547 (b) *Ribbon*, (c) *No IB*, (d) *90eV IB*, (e) *180eV IB* films in "as deposited" state. Dashed

548 lines mark the glass transition temperature.

549

550

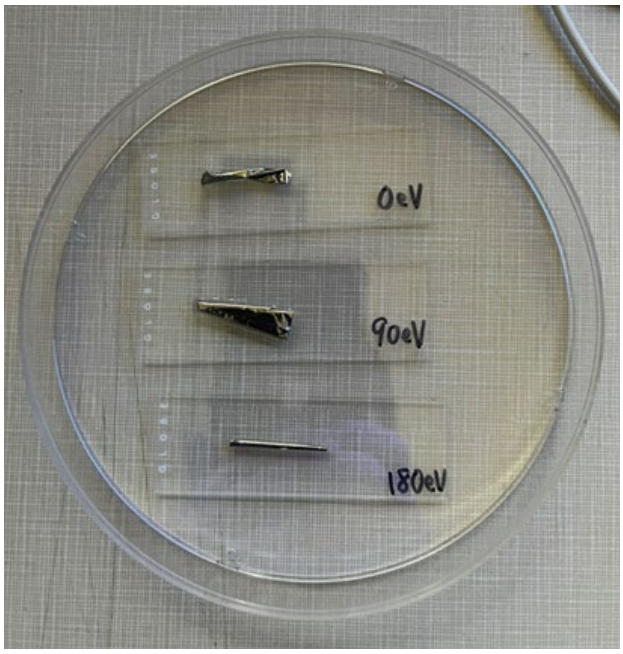

Figure 7. Curling up of the films after being separated from NaCl substrate.

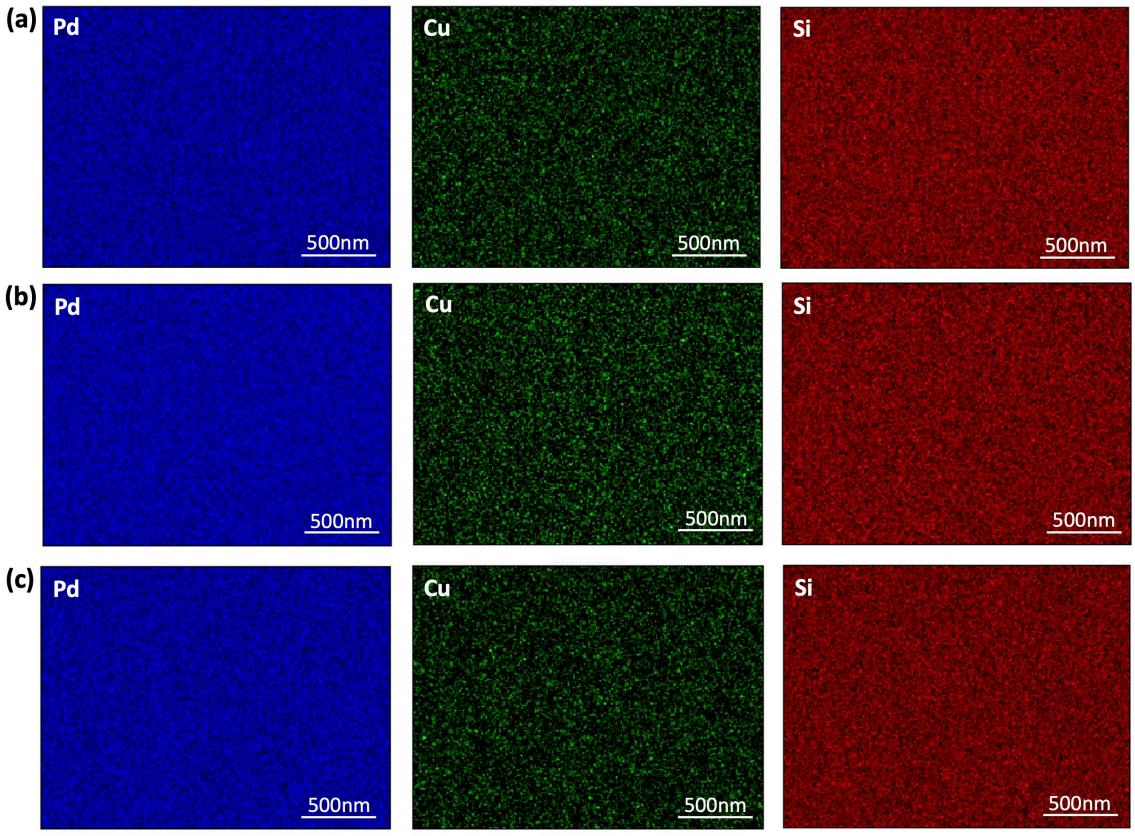

Figure 8. SEM EDS elemental maps for (a) *No IB*, (b) *90eV IB*, and (c)*180eV IB* films showing no microstructural chemical segregation.

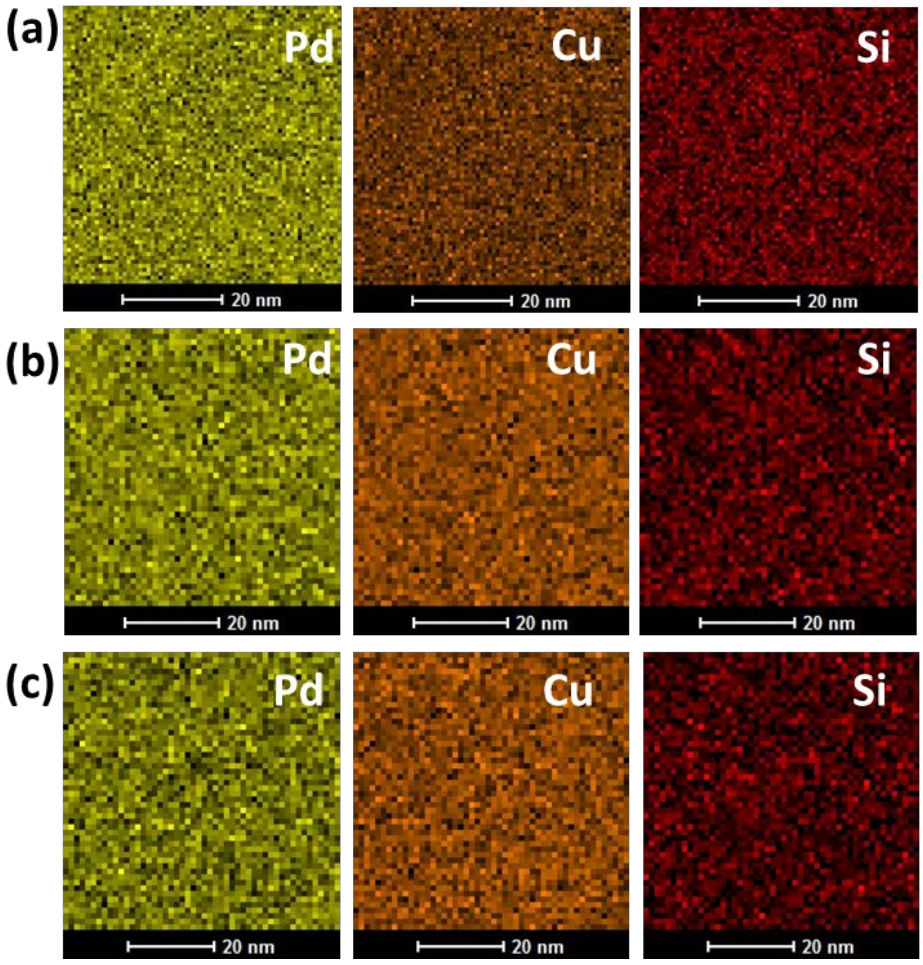

Figure 9. TEM EDS elemental maps for (a) *No IB*, (b) *90eV IB*, and (c)*180eV IB* films showing no nanoscale chemical segregation.

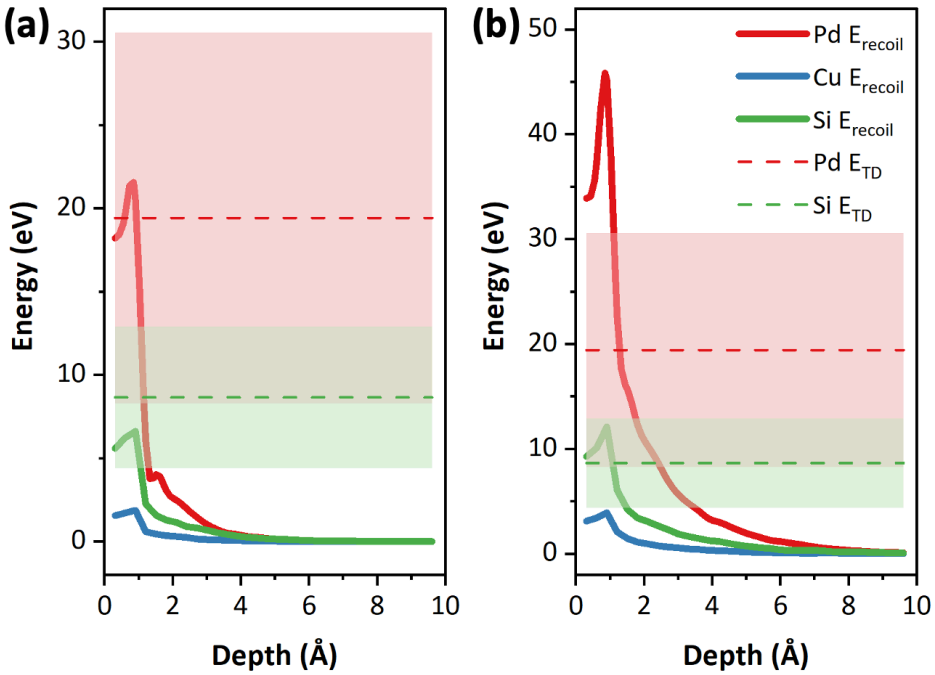

565

566 Figure 10. E_{recoil} (solid) for ion beam energy of (a) 90eV and (b) 180eV compared with

567 threshold displacement energy (E_{TD}) for surface atoms (dashed). Shaded regions

568 represent standard deviations in E_{TD}.